Chirality-dependent scattering of an electron vortex beam by a single atom in a magnetic field

Changyong Lei and Guangjiong Dong

State Key Laboratory of Precision Spectroscopy, East China Normal University, 3663 North Zhongshan Road, Shanghai, China and Collaborative Innovation Center of Extreme Optics, Shanxi University, Taiyuan, Shanxi 030006, China

(Received 28 August 2019; revised 10 February 2021; accepted 22 February 2021; published 12 March 2021)

Electron magnetic circular dichroism (EMCD) can detect the magnetic properties of materials at the nanoscale, but its wide applications are limited by stringent specimen orientation and noisy signal outputs. To overcome these challenges, electron vortex beams (EVBs) were most recently proposed to develop chirality-dependent EMCD (CEMCD), yet convincing and reproducible CEMCD has not yet been demonstrated. In electron energy-loss spectroscopy (EELS) experiments of EMCD, electron-atom scattering has played a core role. Here, from a model research on the scattering of EVBs by a single atom in a magnetic field, we show a way of generating chirality-dependent scattering which is of potential application to CEMCD. The mechanism is to break the symmetry of the joint occupation probability amplitudes for two scattering channels with opposite magnetic quantum number differences (Δm_j), respectively, for two EVBs with opposite topological charges (l). Particularly, the Zeeman effect and spin-orbit coupling jointly can lead to this chirality-dependent scattering, signaled as the chirality-dependent differential cross section (DCS) for the EVB. The DCS can be optimized by choosing the magnetic field strength and topological charge for getting the strongest EMCD. Due to angular momentum conservation, $l = \Delta m_j$ is the optimum topological charge, which could be useful for the selective probe of an internal state. We show that using EVB with a narrow width can relax the requirement of precise controlling of the opening angle and improve the spatial resolution. Finally, we show that chirality-dependent scattering strength decreases with increasing of the impact parameter.

DOI: 10.1103/PhysRevA.103.032815

I. INTRODUCTION

Structured waves in acoustics [1] and optics [2] have produced fruitful applications in bioimaging [3], sensing [4], cooling and trapping of particles [5], and classical and quantum communications [6,7]. Recently, there has been an increasing interest in generating structured matter waves [8–11], and correspondingly new quantum techniques are emerging, for example, electron vortex beams (EVBs) [9–11] could open up chirality-dependent electron magnetic circular dichroism (CEMCD).

Magnetic circular dichroism (MCD) [12], referred to as dichroism induced by an external magnetic field or an intrinsic magnetization, is a powerful method for detecting the magnetic properties of matter in many fields, such as condensed matter physics, and biological physics [13]. Currently, the rapidly expanding spintronics field and nanotechnology as well as biological imaging require reducing the spatial resolution MCD to the nanoscale or even subnanoscale [14–17]. The resolution of well-developed x-ray MCD (XMCD) [18–26] is limited by diffraction. Electrons can have a very short de Broglie wavelength, and their optical properties have been widely used in condensed matter physics [27], biology physics [28], and conventional and cold atomic physics [29], however, its potential for MCD [30] had not been demonstrated until 2006 [31]. Electron MCD (EMCD) [30–32] can offer depth information and an extremely high spatial resolution down to the atomic scale, and thus is drawing increasing interest as an alternative to XMCD. However, the wide application of EMCD has been limited by the precise orientation of a single-crystalline specimen within two or more beams and a low signal-to-noise ratio due to the measurement alongside Bragg spots [33]. Exploiting the intrinsic chirality of EVBs, CEMCD is proposed as an alternative EMCD technique [34,35].

A preliminary electron energy-loss spectroscopy (EELS) experiment of CEMCD [10] has stimulated the theoretical investigations [34–42] of the physical mechanism of generating CEMCD. In EELS experiments, an energy loss above 100 eV implies that the fast incident electron beam is scattered against a core electron of the sample, so the collective effects of the electron gas can be ignored [43], and the scattering processing can be treated as an interaction between an incoming electron and an electron bound by a potential [43], i.e., the EELS experiment of CEMCD can be modeled as a scattering problem of an incident electron beam by an atom [38,44–47]. Reference [41] studies the inelastic interaction of EVB with chiral plasmons or biomolecules and shows that in this situation large transfers of orbital angular momentum (OAM) and a remarkable dichroism in the inelastic interaction of EVB could be possible. However, theoretical investigations in Refs. [36,37,48–51] on scattering of the EVB with a single atom without chirality show that the EELS cannot discriminate the sign of the EVB topological charge, i.e., the chirality of the EVB alone cannot generate CEMCD. A further numerical simulation of the inelastic scattering of EVBs on matter shows [34] that when using a beam size wider than

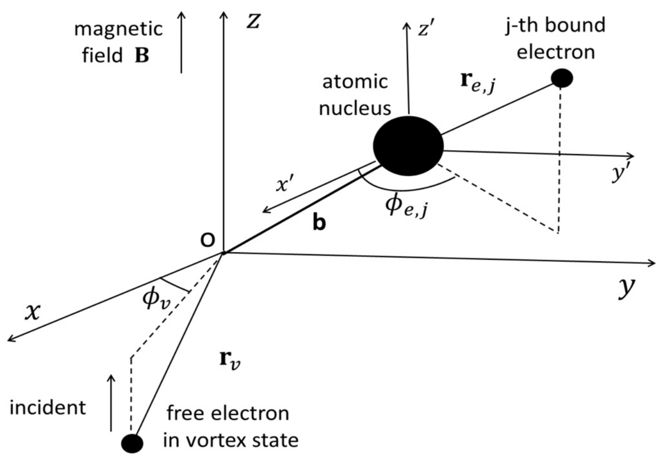

FIG. 1. Schematic of scattering of a flying electron in a vortex state by a fixed atom in a magnetic field **B**. The impact parameter is **b**.

the interatomic separation in the crystal, the energy-filtered diffraction pattern is nearly independent of the EVB topological charge; however, the electron energy spectroscopy is sensitive to the magnetic properties of the target material when channeling the EVB of atomic size through or very close to atomic columns. Thus scattering of narrow EVBs towards an atomic resolution of a magnetic measurement has been explored [35,38,42]. Last year, another scheme using the postselection of both energy and orbital angular momentum of inelastically scattered electrons from a crystalline magnetic sample had been proposed for CEMCD [40]. After significant progress in producing atom-sized EVBs [52–57], a convincing and reproducible CEMCD experiment has not yet been demonstrated [38,58].

In this paper, investigating the inelastic scattering of EVB by an atom in a magnetic field, we theoretically prove that chirality-dependent scattering, of potential application to CEMCD, can be generated by breaking the symmetry of the joint occupation probability amplitudes for two scattering channels with opposite magnetic quantum number differences, respectively, for two EVBs with opposite topological charges. Such a symmetry breaking can be induced by the joint effect of spin-orbit coupling (SOC) and the magnetic field.

This paper is organized as follows. In Sec. II, the differential cross section of an electron vortex by single-atom scattering is derived, and the condition of generating dichroism is proposed. In Sec. III, taking the scattering of a single hydrogen atom in a magnetic field by an electron vortex beam as an example, we show that using the joint effect of spin-orbital coupling and the Zeeman effect, chirality-dependent scattering can be generated and the influence of the magnetic field, incident kinetic energy, opening angle, momentum width, and the impact parameter are numerically investigated. Finally, we give a summary in Sec. IV.

II. THEORY OF INELASTIC SCATTERING OF AN ELECTRON VORTEX BEAM BY A SINGLE ATOM

Our scheme is shown in Fig. 1 where a free electron of mass m_e in a vortex state is incident along the z axis on a fixed atom with nuclei number Z in a magnetic field $\mathbf{B} = B\mathbf{e}_z$, whose nucleus is off the central axis of the electron vortex beam by an impact parameter **b**. The nucleus mass M_n is much larger than the electron mass m_e, and in our theoretical analysis we investigate the inelastic interaction of an electron vortex beam with the bound electron in the atom, neglecting the interaction between the atom nucleus and the EVB due to the weak energy transfer for the forward-scattering electron in electron energy-loss spectroscopy [44]. The Hamiltonian for the EVB-atom interaction system $H = H_v + H_e + H_{\rm int}$ includes the Hamiltonian H_v of an EVB in a magnetic field, the Hamiltonian for the bound electrons of atom H_e, and the interaction Hamiltonian $H_{\rm int}$ between the atom and the EVB. The relativistic effect in general for the swift electron is not significant [59], thus H_v is given by

$$H_v = \mathbf{p}_v^2/(2m_{e,v}) + e(\hat{\mathbf{L}}_v + 2\hat{\mathbf{S}}_v)\cdot\mathbf{B}/(2m_{e,v}), \tag{1}$$

where $\hat{L}_v$ and $\hat{S}_v$ are the orbital and spin angular momentum operators of the EVB, respectively. Here, we have neglected the weak spin-orbital coupling of the vortex electron beam whose strength is about 10^{-13} eV for an EVB with a topological charge 1 [60]. The interaction between the EVB and the atom is dominated by the Coulomb interaction, i.e.,

$$H_{\rm int} = \sum_j e^2/(4\pi\epsilon_0)|\mathbf{r}_v - \mathbf{r}_{e,j} - \mathbf{b}|^{-1}, \tag{2}$$

in which $\mathbf{r}_{e,j}$ is the position vector of the jth bound electron. The weak spin-spin interaction between the EVB and the atom has been neglected. Hereafter, the physical quantities for the incident electron and the bound electron in the atom are distinguished by subscripts v and e, respectively. The Hamiltonian H_e includes the dominant term

$$H_e^0 = \sum_j \left[\hat{\mathbf{p}}_{e,j}^2/(2m_e) - Ze^2/(4\pi\epsilon_0|\mathbf{r}_{e,j}|)\right] + \sum_{i>j} e^2/(4\pi\epsilon_0|\mathbf{r}_{e,i} - \mathbf{r}_{e,j}|), \tag{3}$$

the spin-orbit coupling energy

$$H_{\rm soc} = \delta\sum_j \mathbf{S}_{e,j}\cdot\mathbf{L}_{e,j}/|\mathbf{r}_{e,j}|^3, \tag{4}$$

with the orbital and spin angular momentum of the jth electron of atom $\mathbf{L}_{e,j}$ and $\mathbf{S}_{e,j}$, respectively, the spin-orbit coupling coefficient δ, and the Zeeman energy

$$H_{\rm zm} = \sum_j Z\mu_B B\left(L_{e,z_j} + 2S_{e,z_j}\right)/\hbar, \tag{5}$$

with Bohr magneton μ_B. The spin-orbital coupling $H_{\rm soc}$ and the Zeeman term $H_{\rm zm}$ are treated as perturbation to H_e^0.

The incident wave function for an EVB flying along the z axis in the cylindrical coordinate (ρ_v, φ_v, z_v) is

$$\Psi_i(\mathbf{r}_v) = Nf_l(\rho_v)e^{il\varphi_v}e^{ik_z z_v}\chi_s, \tag{6}$$

where $f_l(\rho_v)$ is the radial distribution of EVB with topological charge l, and the normalization constant is N. $\chi_s = \binom{1}{0}$ for $s = 1/2$, or $\chi_s = \binom{0}{1}$ for $s = -1/2$. When we neglect the spin-spin interaction between the EVB and the bound electron in the atom, the Zeeman effect term in Hamiltonian H_v is commutative with the free-electron Hamiltonian, thus the spin state of the EVB is irrelevant to the scattering processing, and thus, hereafter, we drop off χ_s from the incident wave function.

Typically, the kinetic energy of EVB generated in an electron energy-loss spectroscopy experiment is hundreds of keV [8–11], so the first-order Born approximation [61] can be applied in our analysis [48] for calculating the scattering wave function of an incident plane wave [61]. Thus, to calculate the scattering wave function for the incident EVB, we expand the wave function without including the spin state with plane waves $e^{i\mathbf{k}\cdot\mathbf{r}_v}$, i.e.,

$$\Psi_i(\mathbf{r}_v) = \frac{N}{2\pi i^l}\int a_l(\mathbf{k})e^{il\phi_k}e^{i\mathbf{k}_\perp\cdot\mathbf{r}_v}d^2\mathbf{k}_\perp e^{ik_z z}, \tag{7}$$

in which

$$a_l(\mathbf{k}) \equiv \int f_l(\rho)J_l(k_\perp\rho)\rho d\rho, \tag{8}$$

and ϕ_k is the azimuthal angle of $\mathbf{k}$. Using the quantum superposition principle, the scattering wave function of the EVB by the atom can be treated as the coherent superposition of the scattering spherical wave functions $e^{i\mathbf{k}'\cdot\mathbf{r}_v}/r_v$ of the incident plane waves $e^{i\mathbf{k}\cdot\mathbf{r}_v}$ by the atom according to Eq. (7). In this way, we obtain the scattering wave function of the incident EVB with topological charge l,

$$\Psi_{\rm sc}^{(l)} = -\frac{Nm_e}{4\pi^2\hbar^2 i^l}\int\frac{e^{i\mathbf{k}'\cdot\mathbf{r}_v}}{r_v}e^{il\phi_k}a_l(\mathbf{k})\langle\mathbf{k}',\psi_f'|H_{\rm int}|\mathbf{k},\psi_i\rangle d\mathbf{k}_\perp, \tag{9}$$

in which ψ_i and ψ_f' are the initial and final electronic states of the atom given by the Hamiltonian H_e. $\mathbf{k}'$ is the wave vector of the scattering plane wave. The conservation of energy requires $k'^2 \approx k^2 + 2\sqrt{m_e^2+\hbar^2k^2/c^2}\Delta\varepsilon/\hbar^2$, with $\Delta\varepsilon$ the energy difference of the initial and final atomic states, and

$$\hbar k = \sqrt{\frac{E_k^2}{c^2}+2m_eE_k}, \tag{10}$$

with incident kinetic energy E_k of EVB. Here, the relativistic correction to the swift electron is included [59].

The initial and final atomic states $|\psi_i\rangle$ and $|\psi_f'\rangle$ can be expanded by the unperturbed multielectron atomic eigenstates of H_e^0, $|\beta LSJM_J\rangle$ [62] in which β is an index to represent additional information required to specify the state unambiguously (such as the radial part of the wave function, the parity, and the electronic configuration), L is the total orbital quantum number, S is the total spin quantum number, J is the quantum number for the total angular momentum, and M_J is the projection of $\mathbf{J}$ in the z direction, respectively, i.e.,

$$|\psi_i\rangle = \sum_J C_{\beta LSJM_J}(B)|\beta LSJM_J\rangle, \tag{11}$$

and

$$|\psi_f'\rangle = \sum_{J'} C_{\beta'L'S'J'M_J'}(B)|\beta'L'S'J'M_J'\rangle, \tag{12}$$

where $C_{\beta LSJM_J}(B)$ and $C_{\beta'L'S'J'M_J'}(B)$ are, respectively, the probability amplitudes of occupied states $|\beta LSJM_J\rangle$ and $|\beta'L'S'J'M_J'\rangle$. Now inserting Eqs. (11) and (12) into Eq. (9) we obtain the scattering wave function

$$\Psi_{\rm sc}^{(l)}(\mathbf{r}_v) = -\frac{Ne^{ik_zb_z}}{\pi a_0 i^l}e^{i(l-\Delta M_J)\phi_{k'}}\int\frac{e^{ik'r_v}}{r_v}e^{-i\mathbf{k}'\cdot\mathbf{b}}A(k_\perp)dk_\perp, \tag{13}$$

with the Bohr radius a_0, and the difference of magnetic quantum numbers between the final and initial atomic states

$$\Delta M_J = M_J' - M_J. \tag{14}$$

The scattering amplitude,

$$A(k_\perp) = \sum_{J,J'} W_{\beta LSJM_J}^{\beta'L'S'J'M_J'}T_{\beta LSJM_J}^{\beta'L'S'J'M_J',l}, \tag{15}$$

is the summation of the scattering amplitude for the single scattering channel, $T_{\beta LSJM_J}^{\beta'L'S'J'M_J',l}$, over all scattering channels with the scattering weight probability which is the joint occupation probability amplitude,

$$W_{\beta LSJM_J}^{\beta'L'S'J'M_J'} = C^*_{\beta'L'S'J'M_J'}(B)C_{\beta LSJM_J}(B). \tag{16}$$

Here, the scattering amplitude $T_{\beta LSJM_J}^{\beta'L'S'J'M_J',l}$ is given by

$$T_{\beta LSJM_J}^{\beta'L'S'J'M_J',l} = e^{i\Delta M_J\phi_v}\int M_{fi}(\Delta\mathbf{k})e^{i\mathbf{k}_\perp\cdot\mathbf{b}_\perp}e^{il\phi}d\phi, \tag{17}$$

where

$$M_{fi}(\Delta\mathbf{k}) = \sum_j\langle\beta'L'S'J'\tilde{M}_J|\frac{e^{i\Delta\mathbf{k}\cdot\mathbf{r}_{e,j}}}{|\Delta\mathbf{k}|^2}|\beta LSJ\tilde{M}_J\rangle \tag{18}$$

is the atomic transition matrix element. Applying the Wigner rotation transform which rotates the quantized axis z along the direction of the momentum transfer vector $\Delta\mathbf{k} = \mathbf{k}-\mathbf{k}'$ [63] to Eqs. (18) and (17), we get

$$\begin{aligned} T_{\beta LSJM_J}^{\beta'L'S'J'M_J',l}(k,k') = \sum_j\sum_{q=0}^{|\Delta M_J|}\int_0^{2\pi} & d\phi e^{ik_\perp b_\perp\cos(\phi+\phi_{k'}-\varphi_b)} \\ & \times R_{\beta LSJM_J,j}^{\beta'L'S'J'M_J'}(\mathbf{k},\mathbf{k}',\phi)a_l(\mathbf{k}) \\ & \times \cos\{[l-q\Theta(\Delta M_J)]\phi\}, \end{aligned} \tag{19}$$

with the shape function

$$\begin{aligned} & R_{\beta LSJM_J,j}^{\beta'L'S'J'M_J'}(\mathbf{k},\mathbf{k}',\phi) \\ & = \frac{g_q}{(\Delta k_\perp)^{|\Delta M_J|}}\sum_{\tilde{m}_j=-\min(J',J)}^{\min(J',J)} d_{M_J',\tilde{M}_J}^{(J')}(\tilde{\theta}_{\Delta\mathbf{k}})d_{M_J,\tilde{M}_J}^{(J)}(\tilde{\theta}_{\Delta\mathbf{k}}) \\ & \quad \times\langle\widetilde{\beta'L'S'J'}\tilde{M}_J|\frac{e^{i|\Delta\mathbf{k}|r_{e,j}\cos\theta_{e,j}}}{|\Delta\mathbf{k}|^2}|\widetilde{\beta LSJ}\tilde{M}_J\rangle, \end{aligned} \tag{20}$$

in which

$$g_q = (-1)^{q+|\Delta M_J|}\binom{|\Delta M_J|}{q}k_\perp'^{|\Delta M_J|-q}k_\perp^{q+1}. \tag{21}$$

ϕ is the angle between the scattering wave vector $\mathbf{k}'$ and incident wave vector $\mathbf{k}$, φ_b is the azimuthal angle of $\mathbf{b}$, and $\Theta(\Delta M_J)$ is a sign function. The state vectors $|\beta LSJM_J\rangle$, $|\beta'L'S'J'\tilde{M}_J\rangle$ are transformed into $|\widetilde{\beta LSJ}\tilde{M}_J\rangle$, $|\widetilde{\beta'L'S'J'}\tilde{M}_J\rangle$ by the Wigner rotation transform with rotation angles $\tilde{\phi}_{\Delta\mathbf{k}}$ and

$\tilde{\theta}_{\Delta\mathbf{k}}$. $\tilde{\phi}_{\Delta\mathbf{k}}$ and $\tilde{\theta}_{\Delta\mathbf{k}}$ are, respectively, the azimuthal angle and zenith angle of $\mathbf{\Delta k}$, and the Wigner $d^{(j)}_{m_j,\tilde{m}_j}(\tilde{\theta}_{\Delta\mathbf{k}})$ matrix is defined by Ref. [63].

In Eq. (19), when $l-q\Theta(\Delta M_J)\neq 0$, the value of the oscillatory integration decreases with the increasing of $|l-q\Theta(\Delta M_J)|$, thus the EVB with topological charge $l>0$ prefers to excite the scattering channel with $\Delta M_J>0$; noting that $\cos\{[l-q\Theta(\Delta M_J)]\phi\}=\cos\{[-l-q\Theta(-\Delta M_J)]\phi\}$, thus, on the contrary, the EVB with topological charge $l<0$ tends to excite the scattering channel with $\Delta M_J<0$ more. Especially, when the topological charge l can be equal to $q\Theta(\Delta M_J)$ in Eq. (19), the scattering amplitude $T^{\beta' L'S'J'M_J',l}_{\beta LSJM_J}$ can get higher, and equivalently the momentum conservation requires the EVB of the topological charge l to strongly excite the scattering channel with ΔM_J satisfying $l-q\Theta(\Delta M_J)=0$, as confirmed in the following numerical simulation (cf. Fig. 3).

To make $|\Psi^{(l)}_{\rm sc}(\mathbf{r}_v)|\neq|\Psi^{(-l)}_{\rm sc}(\mathbf{r}_v)|$ (chirality-dependent dichroism), Eqs. (13), (15), (16), and (19) show two possible approaches: In the first approach, if it is possible, we make the transverse shape of EVB in the preparation of the EVB stage in such a way that

$$|f_l(\rho_v)|\neq|f_{-l}(\rho_v)|, \tag{22}$$

such that $a_l\neq a_{-l}$, and consequently $T^{\beta' L'S'J'M_J',l}_{\beta LSJM_J}(k,k')\neq T^{\beta' L'S'J'-M_J',-l}_{\beta LSJ-M_J}(k,k')$, and thus $|\Psi^{(l)}_{\rm sc}(\mathbf{r}_v)|\neq|\Psi^{(-l)}_{\rm sc}(\mathbf{r}_v)|$.

When $a_l=a_{-l}$, $T^{\beta' L'S'J'M_J',l}_{\beta LSJM_J}(k,k')=T^{\beta' L'S'J'-M_J',-l}_{\beta LSJ-M_J}(k,k')$. In this situation, Eq. (15) shows a second way of using an external field to control the internal states to make

$$W^{\beta' L'S'J',-M_J'}_{\beta LSJ,-M_J}\neq W^{\beta' L'S'J',M_J'}_{\beta LSJ,M_J}, \tag{23}$$

i.e., breaking the symmetry of the joint occupation probability amplitudes for two scattering channels with opposite magnetic quantum number differences, respectively, for two EVBs with opposite topological charges.

The dichroism can be demonstrated by measuring the differential cross section. Using Eq. (13), we can obtain the probability flux for the scattered electron by

$$\mathbf{J}_{\rm sc}=i\hbar/(2m_e)[\Psi_{\rm sc}(\mathbf{r}_v)\nabla\Psi^*_{\rm sc}(\mathbf{r}_v)-\Psi^*_{\rm sc}(\mathbf{r}_v)\nabla\Psi_{\rm sc}(\mathbf{r}_v)]. \tag{24}$$

The incident particle flux $\mathbf{J}_{\rm in}=\hbar k_z/(m_eV)\mathbf{e}_z$ [64] for a finite width of EVB in a volume V, and the differential cross section (DCS) [61] $d\sigma^{(l)}_{i\to f}(\mathbf{b})/d\Omega=r_v^2J_{\rm sc}/J_{\rm in}$ is given by

$$\frac{d\sigma^{(l)}_{i\to f}}{d\Omega}=C_f\frac{k'}{k_z}\left|\sum_{J,J'}\int e^{-i\mathbf{k}'\cdot\mathbf{b}}W^{\beta' L'S'J'M_J'}_{\beta LSJM_J}T^{\beta' L'S'J'M_J',l}_{\beta LSJM_J}dk_\perp\right|^2. \tag{25}$$

Here, $C_f=N^2V/(\pi a_0)^2$, and the superscript (l) denotes the dependence of $d\sigma_{i\to f}(\mathbf{b})/d\Omega$ on the topological charge l. When inequality (22) or (23) holds,

$$\frac{d\sigma^{(l)}_{i\to f}(\mathbf{b})}{d\Omega}\neq\frac{d\sigma^{(-l)}_{i\to f}(\mathbf{b})}{d\Omega}, \tag{26}$$

which is an indication of chirality-dependent scattering.

In the above analysis, we have assumed the impact parameter is fixed. But, when the atom can wander in space, we need to include the influence of the probability density of the center of mass $\Phi(\mathbf{b})$. The averaged differential cross section is defined by $d\overline{\sigma}^{(l)}_{i\to f}/d\Omega=\int d\sigma^{(l)}_{i\to f}(\mathbf{b})/d\Omega\Phi(\mathbf{b})d^2\mathbf{b}$, i.e.,

$$\begin{aligned}d\overline{\sigma}^{(l)}_{i\to f}/d\Omega\\&=\frac{N^2V}{2\pi^2a_0^2}\frac{k'}{k_z}\iint d^2\mathbf{k}_\perp d^2\tilde{\mathbf{k}}_\perp a_l(\tilde{\mathbf{k}}_\perp)a_l(\mathbf{k}_\perp)\\&\quad\times[M^*_{fi}(\Delta\tilde{k})M_{fi}(\Delta k)e^{il(\tilde{\phi}-\hat{\phi})}\tilde{\Phi}(\mathbf{k}_\perp-\tilde{\mathbf{k}}_\perp)+\text{c.c.}],\end{aligned} \tag{27}$$

with

$$\tilde{\Phi}(\mathbf{k}_\perp-\tilde{\mathbf{k}}_\perp)=\int e^{i(\mathbf{k}_\perp-\tilde{\mathbf{k}}_\perp)\cdot\mathbf{b}}\Phi(\mathbf{b})d^2\mathbf{b}. \tag{28}$$

Here, c.c. represents the complex conjugate. In the inelastic scattering of EVB, where the wave-packet width of EVB is much less than the momentum transfer vector, we have $|\mathbf{k}-\tilde{\mathbf{k}}|\ll|\Delta\mathbf{k}|\sim|\Delta\tilde{\mathbf{k}}|$, so that we can get

$$\begin{aligned}d\overline{\sigma}^{(l)}_{i\to f}/d\Omega\approx{}&\frac{N^2V}{2\pi^2a_0^2}\frac{k'}{k_z}\iint d^2\mathbf{k}_\perp d^2\tilde{\mathbf{k}}_\perp a_l(\tilde{\mathbf{k}}_\perp)a_l(\mathbf{k}_\perp)\\&\times|M_{fi}(\Delta\mathbf{k})|^2[e^{il(\tilde{\phi}-\hat{\phi})}\tilde{\Phi}(\mathbf{k}_\perp-\tilde{\mathbf{k}}_\perp)+\text{c.c.}].\end{aligned} \tag{29}$$

For the special case $\Phi(\mathbf{b})=\Phi(b)$, i.e., the center-of-mass density is symmetric with respect to the central axis of the vortex beam, from Eq. (29) we have

$$\begin{aligned}d\overline{\sigma}^{(l)}_{i\to f}/d\Omega\approx{}&\frac{N^2V}{\pi^2a_0^2}\frac{k'}{k_z}\iint d^2\mathbf{k}_\perp d^2\tilde{\mathbf{k}}_\perp a_l(\tilde{\mathbf{k}}_\perp)a_l(\mathbf{k}_\perp)\\&\times|M_{fi}(\Delta\mathbf{k})|^2\tilde{\Phi}(|\mathbf{k}_\perp-\tilde{\mathbf{k}}_\perp|)\cos(l\tilde{\phi}'),\end{aligned} \tag{30}$$

where $\tilde{\phi}'=\tilde{\phi}-\hat{\phi}$. Equation (30) shows that when $\Phi(\mathbf{b})=\Phi(b)$ (symmetric trapping of the atoms) and $|a_l(\mathbf{k}_\perp)|=|a_{-l}(\mathbf{k}_\perp)|$ [equivalently, $|f_l(\rho_v)|=|f_{-l}(\rho_v)|$], $d\overline{\sigma}^{(l)}_{i\to f}/d\Omega=d\overline{\sigma}^{(-l)}_{i\to f}/d\Omega$, the averaged DCS with respect to the impact parameter is independent of the sign of the topological charge, agreeing with recent results in Refs. [48–51]. When $|f_l(\rho_v)|=|f_{-l}(\rho_v)|$, in the experiment to observe $d\overline{\sigma}^{(l)}_{i\to f}/d\Omega\neq d\overline{\sigma}^{(-l)}_{i\to f}/d\Omega$, the atom should be anisotropically confined in such a way that $\Phi(\mathbf{b})\neq\Phi(b)$, i.e., the wave function is asymmetric with respect to the central axis of the vortex beam. We should note that when $|f_l(\rho_v)|\neq|f_{-l}(\rho_v)|$, even in the case of $\Phi(\mathbf{b})=\Phi(b)$, the averaged differential cross section $d\overline{\sigma}^{(l)}_{i\to f}/d\Omega\neq d\overline{\sigma}^{(l)}_{i\to f}/d\Omega$ can be generated.

Possibly, some works have already generated a chirality-broken amplitude of EVBs, for example, Fig. 3 in Ref. [65] shows $|f_l(\rho_v)|\neq|f_{-l}(\rho_v)|$, but this feature has not been explored for CEMCD experiments. So far, how to make a chirality-broken amplitude of EVB wave functions [Eq. (22)] is not clear and will not be further explored in this paper. Hereafter, we focus on the second way. Without including SOC and the Zeeman effect [36,37,48], the condition (23) cannot be met. When solely including the Zeeman effect in the analysis, though energy levels can be split due to the Zeeman effect, the spatial wave function cannot be changed, and thus the condition (23) cannot be met. When SOC is included in the analysis but without the Zeeman effect, though the energy levels are split, the weight factors $C_{\beta LS(L\pm S)M_J} = C_{\beta LS(L\pm S)(-M_J)}$, which cannot lead to the condition (23). When both the Zeeman effect and SOC are added, $C_{\beta LS(L\pm S)M_J}$ is magnetic field dependent, and especially $C_{\beta LS(L\pm S)M_J} \neq C_{\beta LS(L\pm S)(-M_J)}$, resulting in the satisfaction of the condition (23).

III. NUMERICAL RESULTS OF CHIRALITY-DEPENDENT SCATTERING OF AN EVB BY A SINGLE ATOM

Now, we take a hydrogenlike atom as the target atom to illustrate chirality-dependent scattering. The SOC [62] can split the eigenstate of H_e^0 into two branches as shown in Fig. 2, where the splitting of $1s$ and $2p$ states of a hydrogen atom in a magnetic field is plotted, and the magnetic field further fully lifts off the degeneracy. Using the perturbation theory [62], the corresponding perturbed wave functions are given by

$$\left|\psi^p_{n\ell m_j}\right\rangle = \sum_{j=\ell\pm 1/2} C^p_{n\ell s j m_j}(B)|n\ell s j m_j\rangle, \tag{31}$$

where $p = 1, 2$ denotes the branches of the split energy levels (lowercase letters, rather than capital letters, are used for the quantum number of a single electron atom as in conventional textbooks, and n is the principal quantum number), and the probability amplitudes are

$$\begin{aligned} C^1_{n\ell s,\ell\pm 1/2,m_j} &= \pm\sqrt{(1\pm D_{n\ell m_j\gamma})/2}, \\ C^2_{n\ell s,\ell\pm 1/2,m_j} &= \sqrt{(1\mp D_{n\ell m_j\gamma})/2}, \end{aligned} \tag{32}$$

with

$$D_{n\ell m_j\gamma} = 1\Big/\sqrt{1+\frac{1-(2m_j/\ell_r)^2}{[\ell_r/(2\ell\gamma)+2m_j/\ell_r]^2}}, \tag{33}$$

where $\ell_r = 2\ell + 1$,

$$\gamma = \mu_B B/\varepsilon_{n,\ell} \tag{34}$$

is the ratio of Zeeman energy to SOC energy, and

$$\varepsilon_{n,\ell} = \alpha^4 m_e c^2/[n^3\ell_r(\ell+1)]. \tag{35}$$

Using $C_{\beta LSJM_J}(B)$, $C_{\beta' L'S'J'M_J'}(B)$ in Eq. (16), we have calculated the scattering weight probability $W^{n'\ell's'j'm_j'}_{n\ell s j m_j}$. For example, for the transition $1s_{1/2,1/2} \to 2p_{3/2,-1/2}$ ($\Delta m = -1$),

$$W^{21\frac{1}{2}\frac{3}{2}-\frac{1}{2}}_{10\frac{1}{2}\frac{1}{2}\frac{1}{2}} = \sqrt{\frac{1+\frac{1}{\sqrt{1+8/(9/\gamma-1)^2}}}{2}} + \sqrt{1-\frac{1}{\sqrt{1+8/(9/\gamma-1)^2}}}, \tag{36}$$

and for the $1s_{1/2,-1/2} \to 2p_{3/2,1/2}$ ($\Delta m = 1$),

$$W^{21\frac{1}{2}\frac{3}{2}\frac{1}{2}}_{10\frac{1}{2}\frac{1}{2}-\frac{1}{2}} = \sqrt{\frac{1+\frac{1}{\sqrt{1+8/(9/\gamma+1)^2}}}{2}} - \sqrt{1-\frac{1}{\sqrt{1+8/(9/\gamma+1)^2}}}. \tag{37}$$

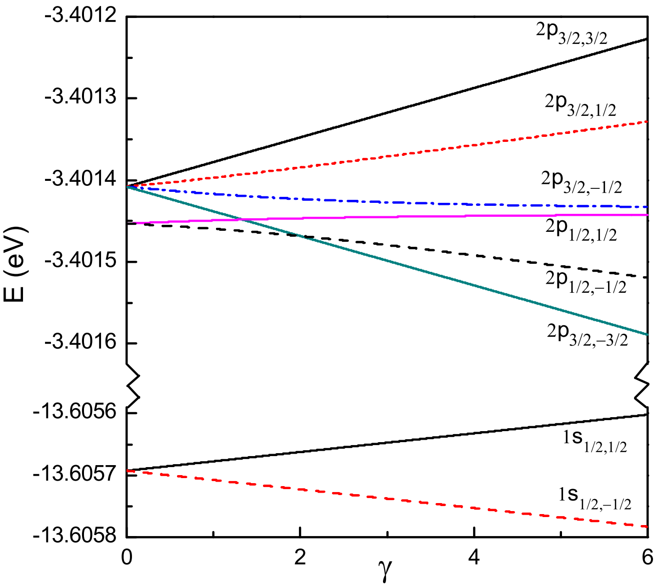

FIG. 2. Splitting $1S$ states (bottom) and $2P$ states (top) of a hydrogenlike atom with the ratio of Zeeman energy to SOC energy γ.

From the analysis of Eq. (19), $1s_{1/2,1/2} \to 2p_{3/2,-1/2}$ ($\Delta m = -1$) is a favored scattering channel by the EVB with $l < 0$, and $1s_{1/2,-1/2} \to 2p_{3/2,1/2}$ ($\Delta m = 1$) is a scattering channel more excited by the EVB with $l > 0$. Without the magnetic field ($\gamma = 0$) or not including the spin-orbital coupling ($\gamma = \infty$), $W^{21\frac{1}{2}\frac{3}{2}-\frac{1}{2}}_{10\frac{1}{2}\frac{1}{2}\frac{1}{2}} = W^{21\frac{1}{2}\frac{3}{2}\frac{1}{2}}_{10\frac{1}{2}\frac{1}{2}-\frac{1}{2}}$; however, for a finite $\gamma > 0$, $W^{21\frac{1}{2}\frac{3}{2}-\frac{1}{2}}_{10\frac{1}{2}\frac{1}{2}\frac{1}{2}} \neq W^{21\frac{1}{2}\frac{3}{2}\frac{1}{2}}_{10\frac{1}{2}\frac{1}{2}-\frac{1}{2}}$. We find that the joint effect of SOC and the Zeeman effect leads to the condition (23).

Taking transitions from $1s_{1/2} \to 2p_{3/2}$ and $1s_{1/2} \to 3d_{5/2}$ excited by EVBs with $\pm l$ as examples, we study the chirality-dependent scattering quantitatively. For an ideal Bessel beam, $a_l(\mathbf{k}) \sim \delta(k_\perp - k_{\perp,0})/k_\perp$, but for the experimentally generated EVB, the momentum distribution cannot be so sharp. In the following calculation, we adopt a model recently proposed in Ref. [66], where $a_l(\mathbf{k})$ is given by [66]

$$a_l(\mathbf{k}) = \sqrt{\frac{2}{\sqrt{\pi}\sigma}}\,\frac{e^{-\frac{(k_\perp - k_{\perp,0})^2}{2\sigma^2}}}{k_\perp}, \tag{38}$$

with e^{-1} the width of the momentum density σ, and the central transverse momentum $k_{\perp,0}$. According to this model, $a_l(\mathbf{k})$ is l independent, and when $\sigma \to 0$, $a_l(\mathbf{k})$ approaches the momentum distribution for the ideal Bessel beam. In the numerical calculation, the incident kinetic energy E_k of EVB is 200 keV, and the impact vector $\mathbf{b}$ is along the x axis ($\varphi_b = 0$). Due to the magnetic field and SOC, the energy levels are split, the atom is scattered from the fine state of the ground state to the fine state of the excited state, i.e., the initial state $|i\rangle$ and final state $|f\rangle$ are the fine states, thus $d\sigma^{(l)}(\mathbf{b})/d\Omega = \sum_{i,f}\sigma^{(l)}_{i\to f}(\mathbf{b})/d\Omega$. Figure 3 studies the relation of the DCS difference, $S(\theta) \equiv d\sigma^{(-l)}(\mathbf{b})/d\Omega - d\sigma^{(l)}(\mathbf{b})/d\Omega$, to the scattering angle θ for $l = 1$, 2, and 3, opening angle $\alpha \equiv \arctan(k_{\perp,0}/k_z) = 0.1$ mrad, wave-packet width $\sigma = 0.01a_0^{-1}$, and $\gamma = 0.5, 4, 9$, and 100 [67]. When $\gamma \ll 1$ ($B \approx 0$), SOC is

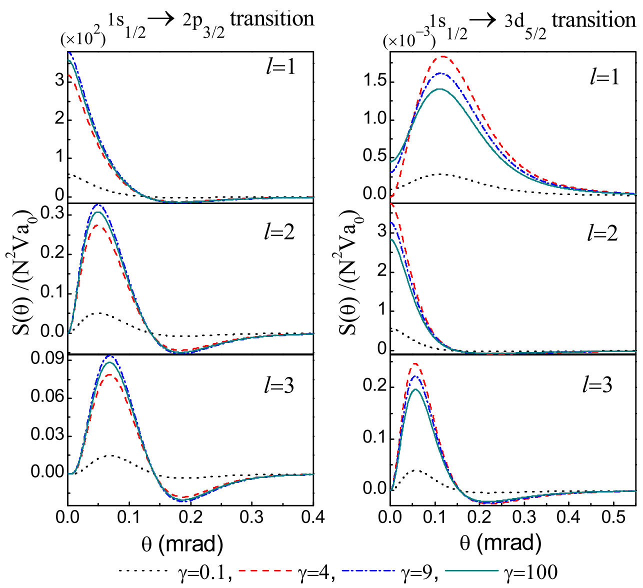

FIG. 3. The angular distribution of DSCS difference $S(\theta)$ for different magnetic field strengths $\gamma = 0.5$ (black dotted line), $\gamma = 4$ (red dashed line), $\gamma = 9$ (blue dashed-dotted line), and $\gamma = 100$ (dark-cyan solid line) with $l = 1$, 2, and 3 are shown, respectively. The atomic transitions $1s_{1/2} \to 2p_{3/2}$ (left panel) and $1s_{1/2} \to 3d_{5/2}$ (right panel) are considered here. Other parameters: EVB opening angle $\alpha = 0.1$ mrad and wave-packet width $\sigma = 0.01a_0^{-1}$, impact parameter $b = a_0$, and the incident kinetic energy of EVB, $E_k = 200$ keV.

dominant, $S(\theta) \approx 0$, and chirality-dependent scattering can be hardly generated. With increasing γ, the Zeeman effect starts to play, and the DCS difference increases until it reaches its maximum around $\gamma_m \approx 9$ for $1s_{1/2} \to 2p_{3/2}$ ($B \approx 4.7$ T) and $\gamma_m \approx 4$ for $1s_{1/2} \to 3d_{5/2}$ ($B \approx 0.25$ T). When γ increasing crosses over the γ_m for the maximum of DCS differences, the Zeeman effect dominates, and further increasing γ drives the atom into the Paschen-Back region [62] and thus the chirality-dependent scattering effect is reduced. Thus, Fig. 3 shows there is an l-dependent optimum magnetic field strength.

Figure 3 shows that for the same transition, there is an optimum topological charge l to achieve the maximum $S(\theta)$. Actually, when $l - q\Theta(\Delta m_j) \neq 0$ in Eq. (19), the oscillatory integration in this equation leads to the decreasing of the scattering amplitude for the single scattering channel with topological charge l. When $l - q\Theta(\Delta m_j) = 0$ in Eq. (19), this implies the orbital angular momentum of the swift vortex electron can meet the requirement of the angular momentum conservation for the transition. For the $1s_{1/2} \to 2p_{3/2}$ transition, $\Delta m_j = \pm 1$, thus the maximum $S(\theta)$ can be achieved for the topological charge $l = \mp 1$. For the $1s_{1/2} \to 3d_{5/2}$ transition, $\Delta m_j = \pm 1, \pm 2$, thus $S(\theta)$ for $l = \mp 1$ is compatible to that for $l = \mp 2$, while the latter (right panel of Fig. 3) is higher, because the scattering weight probability$|W_{n\ell s j m_j}^{n'\ell' s' j' m_j'}|$ for $\Delta m_j = \pm 2$ is higher than that for $\Delta m_j = \pm 1$. Thus, we can use EVB with different topological charges l to distinguish the internal energy levels. Recently, there has been growing interest in generating EVBs with topological charges much larger than 1 [11,68–71]. We note that the magnitude of

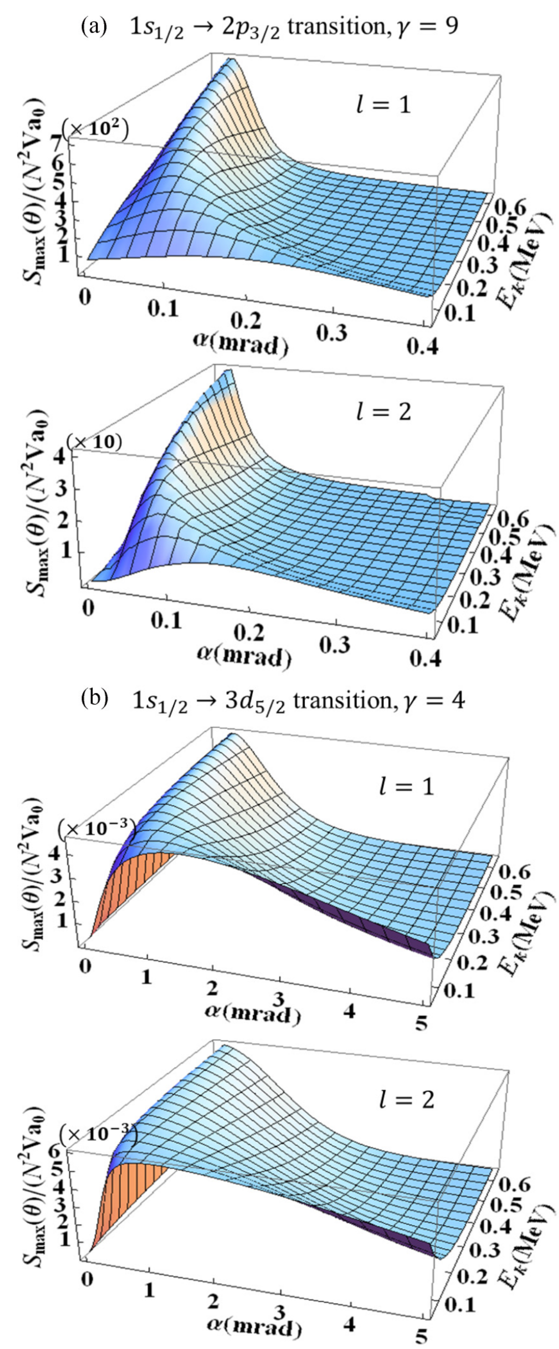

FIG. 4. The peak value of the angular distribution of the DSCS difference $S_{\max}(\theta)$ vs opening angle α and the incident kinetic energy E_k of EVBs with wave-packet width $\sigma = 0.01a_0^{-1}$ and impact parameter $b = a_0$ is plotted for (a) the transition $1s_{1/2} \to 2p_{3/2}$ with the ratio of the Zeeman energy over the spin-coupling energy $\gamma = 9$ and (b) $1s_{1/2} \to 3d_{5/2}$ transition with $\gamma = 4$, respectively.

$S(\theta)$ for the transition to a higher state, i.e., $1s_{1/2} \to 3d_{5/2}$, is much lower than that for the lower state, e.g., $1s_{1/2} \to 2p_{3/2}$, as shown in Fig. 3, and as a result the shape function $R_{n\ell s j m_j, q}^{n'\ell' s' j' m_j'}$ defined by Eq. (20) decreases with the energy loss. Therefore, it is not necessary to use an extremely high topological charge to probe the low-lying states.

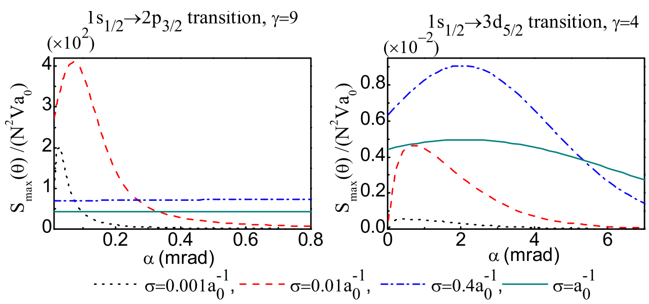

FIG. 5. Controlling $S_{\max}(\theta)$ with opening angle α for different wave-packet momentum widths $\sigma = 0.001a_0^{-1}, 0.01a_0^{-1}, 0.4a_0^{-1}$, and $1a_0^{-1}$. The optimum magnetic fields are used for each transition channel, impact parameter $b = a_0$, topological charge $l = 1$, and $E_k = 200$ keV.

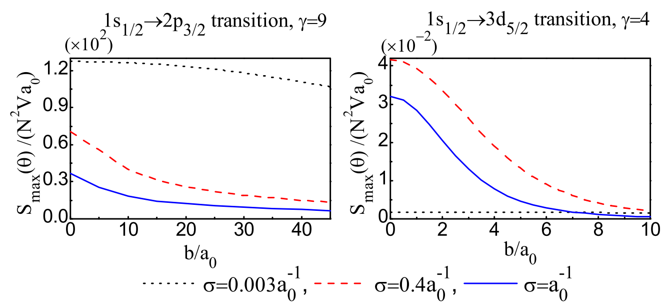

FIG. 6. $S_{\max}(\theta)$ vs the impact parameter b for different wave-packet momentum widths $\sigma = 0.003a_0^{-1}$, $0.4a_0^{-1}$, and a_0^{-1}. The optimum magnetic fields, opening angles $\alpha = 0.1$ mrad (left panel) and 0.4 mrad (right panel), $E_k = 200$ keV, and topology charges $l = 1$ (left panel) and 2 (right panel) are used.

According to Eq. (9), the scattering wave function of the EVB by the atom is a coherent superposition of the scattering wave functions of the incident plane waves composing $e^{i\mathbf{k}\cdot\mathbf{r}_v}$ of the EVB according to Eq. (7). As a result, constructive interference of the scattered spherical electron waves $e^{i\mathbf{k}'\cdot\mathbf{r}_v}/r_v$ can be generated in a specific scattering angle, thus Fig. 3 shows that there is a scattering angle that $S(\theta)$ can get the maximum value $S_{\max}(\theta)$.

The relation of the peak value of DCS differences $S_{\max}(\theta)$ to the incident kinetic energy E_k and opening angle α of EVBs with topological charges $l = 1$ and 2 is shown in Fig. 4, respectively, for the $1s_{1/2} \rightarrow 2p_{3/2}$ transition with $\gamma = 9$ [Fig. 4(a)] and the $1s_{1/2} \rightarrow 3d_{5/2}$ transition with $\gamma = 4$ [Fig. 4(b)] calculated with a wave-packet width $\sigma = 0.01a_0^{-1}$ and impact parameter $b = a_0$. For a given incident kinetic energy, there is an optimum opening angle, denoted as α_o. When α is off from α_o, $S_{\max}(\theta)$ quickly decays. The optimum opening angle α_o is different for different transitions ($1s_{1/2} \rightarrow 2p_{3/2}$ transition, and $1s_{1/2} \rightarrow 3d_{5/2}$ transition).

The momentum width σ of the EVB is another important parameter for controlling the scattering, as confirmed in Fig. 5, where the relation of $S_{\max}$ to α and σ is investigated for the EVB with $E_k = 200$ keV. $S_{\max}$ gets its highest value at $\alpha = 0.1$ mrad and $\sigma = 0.01a_0^{-1}$ for the $1s_{1/2} \rightarrow 2p_{3/2}$ transition (left panel in Fig. 5), the corresponding average transverse radius $\langle\rho\rangle = \int |\Psi_i(\mathbf{r}_v)|^2 \rho d^3 r_v$ of the incident EVB is numerically found to be about 16 nm. There is a similar feature for the $1s_{1/2} \rightarrow 3d_{5/2}$ transition (right panel in Fig. 5), where the curve $S_{\max}$ gets its maximum value at $\sigma = 0.4a_0^{-1}$ and $\alpha = 0.4$ mrad. Therefore, there is an optimum beam size for getting the strongest CEMCD signal. On the other hand, pursuing the strongest signal faces the challenge of precise controlling of the opening angle. For a relatively narrow momentum distribution σ, for example, in the $1s_{1/2} \rightarrow 2p_{3/2}$ transition, $\sigma \leqslant 0.01a_0^{-1}$, the $S_{\max}$-α curve has a narrow peak width ($\lesssim$0.1 mrad), such that it is hard to detect CEMCD when α deviates slightly from the peak position. Increasing the momentum distribution ($\sigma \geqslant 0.4a_0^{-1}$), equivalently reducing the EVB width, the $S_{\max}$ vs α curves are nearly flat for a relatively large range ($\sim$1 mrad) of α, thus the requirement of precise controlling of the opening angle can be relaxed. In contrast, the $S_{\max}$ vs α curves for the $1s_{1/2} \rightarrow 3d_{5/2}$ transition (right panel in Fig. 5) have a larger momentum width σ ($\geqslant a_0^{-1}$) which relatively relaxes the precise controlling of the opening angle.

In Fig. 6, $S_{\max}$ versus the impact parameter b is shown. $S_{\max}$ decreases with the increasing of the impact parameter b for both $1s_{1/2} \rightarrow 2p_{3/2}$ (left panel) and $1s_{1/2} \rightarrow 3d_{5/2}$ (right panel) transitions. Moreover, with increasing momentum width σ, equivalently reducing the wave-packet width, $S_{\max}$ strongly decreases with b. In this sense, it is better to use a relatively larger wave-packet width to reduce the off-center effect.

IV. SUMMARY

In summary, we have obtained the differential cross section for the scattering of an EVB by an atom using the Born approximation. The total scattering amplitude is the summation of the scattering amplitude over the entire scattering channel with a scattering weight probability which is the joint probability amplitude occupying the initial state and the final state in a single scattering channel. When the symmetry of the scattering weight probability for a single channel of the EVB with a topological charge l between that for its counterpart of the EVB with a topological charge $-l$ is breaking, chirality-dependent scattering can be generated. Such a symmetry breaking can be realized in the presence of SOC and the Zeeman effect. In this approach, chirality-dependent scattering can be optimized by choosing the proper magnetic field strength and topological charge, incident energy, as well as beam size. Especially, using a narrow beam size, the requirement of precise controlling of the opening angle can be relaxed. The optimum topological charge l of EVB for realizing chirality-dependent scattering is $l = \Delta m_j$, thus we can use EVBs with different topological charges to selectively probe the atomic internal states. When the atom is off center of the EVB, the dichroism decreases with increasing of the impact parameter **b**. We also propose one approach to induce CEMCD by breaking the chiral symmetry of the incident EVB wave function.

Chirality-dependent scattering could be applied to generate CEMCD [38,46]. The scattering theory in this paper should be modified by taking account of the distortion of the EVB within a crystal [72]. To detect the magnetic properties, the magnetic field in our analysis should be modified to include the local magnetic field of the magnetic material.

Our theory can be further extended from a single atom to ultracold gas dynamics to explore the possibility of chirality-dependent scanning electron microscopy of ultracold gases [29,73,74], an important tool for manipulating and probing ultracold gas dynamics, particularly for probing the quantum magnetism of spinor gases.

ACKNOWLEDGMENTS

G.D. thanks Professor Weiping Lu for improving the manuscript. G.D. acknowledges support from the Innovation Program of Shanghai Municipal Education Commission (Grant No. 2019-01-07-00-05-E00079) the National Science Foundation of China (Grants No. 11574085, No. 91536218, and No. 11834003), the National Key Research and Development Program of China (Grant No. 2017YFA0304201), and Overseas Expertise Introduction Project for Discipline Innovation (No. B12024).

[1] A. Marzo, M. Caleap, and B. W. Drinkwater, Phys. Rev. Lett. **120**, 044301 (2018).

[2] H. Rubinsztein-Dunlop *et al.*, J. Opt. **19**, 013001 (2017).

[3] L. Y. Shi, L. Lindwasser, W. B. Wang, R. Alfano, and A. Roddriguez-Contreras, J. Biophotonics **10**, 1756 (2017); W. Brullot, M. K. Vanbel, T. Swusten, and T. Verbiest, Sci. Adv. **2**, e1501349 (2016).

[4] A. Belmonte, C. Rosales-Guzman, and J. P. Torres, Optica **2**, 1002 (2015).

[5] A. R. Carter, M. Babiker, M. Al-Amri, and D. L. Andrews, Phys. Rev. A **73**, 021401(R) (2006); A. R. Carter and M. Babiker, *ibid.* **77**, 043401 (2008).

[6] M. Mirhosseini, O. S. Magaña-Loaiza, M. N. O'Sullivan, B. Rodenburg, M. Malik, M. P. J. Lavery, M. J. Padgett, D. J. Gauthier, and R. W. Boyd, New J. Phys. **17**, 033033 (2015).

[7] L. Gong, Q. Zhao, H. Zhang, X.-Y. Hu, K. Huang, J.-M. Yang, and Y.-M. Li, Light: Sci. Appl. **8**, 27 (2019).

[8] K. Y. Bliokh, Y. P. Bliokh, S. Savel'ev, and F. Nori, Phys. Rev. Lett. **99**, 190404 (2007).

[9] M. Uchida and A. Tonomura, Nature (London) **464**, 737 (2010).

[10] J. Verbeeck, H. Tian, and P. Schattschneider, Nature (London) **467**, 301 (2010).

[11] B. J. McMorran, A. Agrawal, I. M. Anderson, A. A. Herzing, H. J. Lezec, J. J. McClelland, and J. Unguris, Science **331**, 192 (2011).

[12] D. Caldwell, J. M. Thorne, and H. Eyring, Annu. Rev. Phys. Chem. **22**, 259 (1971); T. Funk, A. Deb, S. J. George, H. X. Wang, and S. P. Cramer, Coord. Chem. Rev. **249**, 3 (2005).

[13] J. C. Sutherland and B. Holmquist, Annu. Rev. Biophys. Bioeng. **9**, 293 (1980).

[14] G. Van Tendeloo, S. Bals, S. Van Aert, J. Verbeeck, and D. Van Dyck, Adv. Mater. **24**, 5655 (2012).

[15] J. Rusz, S. Muto, J. Spiegelberg, R. Adam, K. Tatsumi, D. E. Bürgler, P. M. Oppeneer, and C. M. Schneider, Nat. Commun. **7**, 12672 (2016).

[16] P. Schattschneider, M. Stöger-Pollach, S. Rubino, M. Sperl, C. Hurm, J. Zweck, and J. Rusz, Phys. Rev. B **78**, 104413 (2008).

[17] D. Nolle, M. Weigand, G. Schütz, and E. Goering, Microsc. Microanal. **17**, 834 (2011).

[18] G. Schütz, W. Wagner, W. Wilhelm, P. Kienle, R. Zeller, R. Frahm, and G. Materlik, Phys. Rev. Lett. **58**, 737 (1987).

[19] G. van der Laan, J. Magn. Magn. Mater. **156**, 99 (1996).

[20] B. T. Thole, G. van der Laan, and G. A. Sawatzky, Phys. Rev. Lett. **55**, 2086 (1985).

[21] B. T. Thole, P. Carra, F. Sette, and G. van der Laan, Phys. Rev. Lett. **68**, 1943 (1992).

[22] P. Carra, B. T. Thole, M. Altarelli, and X. D. Wang, Phys. Rev. Lett. **70**, 694 (1993).

[23] P. Kuiper, B. G. Searle, P. Rudolf, L. H. Tjeng, and C. T. Chen, Phys. Rev. Lett. **70**, 1549 (1993).

[24] G. van der Laan and B. T. Thole, Phys. Rev. B **43**, 13401 (1991).

[25] C. T. Chen, Y. U. Idzerda, H-J. Lin, N. V. Smith, G. Meigs, E. Chaban, G. H. Ho, E. Pellegrin, and F. Sette, Phys. Rev. Lett. **75**, 152 (1995).

[26] A. Ankudinov and J. J. Rehr, Phys. Rev. B **51**, 1282 (1995).

[27] J. Zabloudil, D. R. Hammerling, P. Weinberger, and L. Szunyogh, *Electron Scattering in Solid Matter: A Theoretical and Computational Treatise* (Springer, Berlin, 2005).

[28] M. Hayat, *Principles and Techniques of Electron Microscopy, Biological Applications*, 4th ed. (Cambridge University Press, Cambridge, U.K., 2000).

[29] B. Santra and H. Ott, J. Phys. B: At., Mol. Opt. Phys. **48**, 122001 (2015).

[30] C. Hébert and P. Schattschneider, Ultramicroscopy **96**, 463 (2003).

[31] P. Schattschneider, S. Rubino, C. Hébert, J. Rusz, J. Kuneš, P. Novák, E. Carlino, M. Fabrizioli, G. Panaccione, and G. Rossi, Nature (London) **441**, 486 (2006).

[32] P. Schattschneider, S. Rubino, M. Stoeger-Pollach, C. Hébert, J. Rusz, L. Calmels, and E. Snoeck, J. Appl. Phys. **103**, 07D931 (2008).

[33] S. Rubinoa, P. Schattschneider, M. Stöer-Pollach, C. Hébert, J. Rusz, L. Calmels, B. Warot-Fonrose, F. Houdellier, V. Serin, and P. Novak, J. Mater. Research **23**, 2582 (2008).

[34] J. Rusz and S. Bhowmick, Phys. Rev. Lett. **111**, 105504 (2013).

[35] J. Rusz, S. Bhowmick, M. Eriksson, and N. Karlsson, Phys. Rev. B **89**, 134428 (2014).

[36] S. M. Lloyd, M. Babiker, and J. Yuan, Phys. Rev. Lett. **108**, 074802 (2012).

[37] S. M. Lloyd, M. Babiker, and J. Yuan, Phys. Rev. A **86**, 023816 (2012).

[38] P. Schattschneider, S. Löffler, M. Stöge-Pollach, and J. Verbeeck, Ultramicroscopy **136**, 81 (2014).

[39] T. Schachinger, S. Löffler, A. Steiger-Thirsfeld, M. Stöger-Pollach, S. Schneider, D. Pohl, B. Rellinghaus, and P. Schattschneider, Ultramicroscopy **179**, 15 (2017).

[40] E. Rotunno, M. Zanfrognini, S. Frabboni, J. Rusz, R. E. Dunin Borkowski, E. Karimi, and V. Grillo, Phys. Rev. B **100**, 224409 (2019).

[41] A. Asenjo-Garcia and F. J. García de Abajo, Phys. Rev. Lett. **113**, 066102 (2014).

[42] J. Rusz, J.-C. Idrobo, and S. Bhowmick, Phys. Rev. Lett. **113**, 145501 (2014).
[43] P. Schattschneider, *Linear and Chiral Dichroism in the Electron Microscope* (CRC Press/Taylor & Francis, Boca Raton, FL, 2011).
[44] D. A. Muller and J. Silcox, Ultramicroscopy **59**, 195 (1995).
[45] P. Schattschneider, J. Verbeeck, and A. L. Hamon, Ultramicroscopy **109**, 781 (2009).
[46] P. Schattschneider, J. Verbeeck, V. Mauchamp, M. Jaouen, and A. L. Hamon, Phys. Rev. B **82**, 144418 (2010).
[47] M. Schüler and J. Berakdar, Phys. Rev. A **94**, 052710 (2016).
[48] R. Van Boxem, B. Partoens, and J. Verbeeck, Phys. Rev. A **91**, 032703 (2015).
[49] V. Serbo, I. P. Ivanov, S. Fritzsche, D. Seipt, and A. Surzhykov, Phys. Rev. A **92**, 012705 (2015).
[50] R. Van Boxem, B. Partoens, and J. Verbeeck, Phys. Rev. A **89**, 032715 (2014).
[51] A. L. Harris, A. Plumadore, and Z. Smozhanyk, J. Phys. B: At., Mol. Opt. Phys. **52**, 094001 (2019).
[52] O. L. Krivanek, J. Rusz, J.-C. Idrobo, T. J. Lovejoy, and N. Dellby, Microsc. Microanal. **20**, 832 (2014).
[53] J. Verbeeck, P. Schattschneider, S. Lazar, M. Stöer-Pollach, S. Löffler, A. Steiger-Thirsfeld, and G. V. Tendeloo, Appl. Phys. Lett. **99**, 203109 (2011).
[54] P. Schattschneider, M. Stöger-Pollach, S. Löffler, A. Steiger-Thirsfeld, J. Hell, and J. Verbeeck, Ultramicroscopy **115**, 21 (2012); D. Pohl, S. Schneider, P. Zeiger, J. Rusz, P. Tiemeijer, S. Lazar, K. Nielsch, and B. Rellinghaus, Sci. Rep. **7**, 934 (2017).
[55] A. Béché, R. V. Boxem, G. V. Tendeloo, and J. Verbeeck, Nat. Phys. **10**, 26 (2014).
[56] A. Béché, R. Juchtmans, and J. Verbeeck, Ultramicroscopy **178**, 12 (2017).
[57] D. S. Negi, J.-C. Idrobo, and J. Rusz, Sci. Rep. **8**, 4019 (2018).
[58] D. Pohl, S. Schneider, J. Rusz, and B. Rellinghaus, Ultramicroscopy **150**, 16 (2015).
[59] As written in Ref. [43], "In an electron energy loss spectrometry (EELS) experiment in a transmission electron microscope (TEM), fast electrons (in general 80 to 300 keV) are used as probe particles. Their kinetic energy corresponds to electron velocities of 50 to 80% of the light velocity. One would expect to see relativistic effects in the experiment. Surprisingly, apart from the replacement of the electron's rest mass by the relativistic mass, the non-relativistic quantum mechanical expressions for the scattering process hold in the majority of cases."
[60] S. M. Lloyd, M. Babiker, J. Yuan, and C. Kerr-Edwards, Phys. Rev. Lett. **109**, 254801 (2012).
[61] H. Schober, J. Neutron Research **17**, 109 (2014).
[62] M. Weissbluth, *Atoms and Molecules* (Academic, New York, 1978).
[63] R. Zare, *Angular Momentum* (Wiley, New York, 1988).
[64] U. D. Jentschura and V. G. Serbo, Eur. Phys. J. C **71**, 1571 (2011).
[65] A. Rajabi and J. Berakdar, Phys. Rev. A **95**, 063812 (2017).
[66] D. V. Karlovets, G. L. Kotkin, V. G. Serbo, and A. Surzhykov, Phys. Rev. A **95**, 032703 (2017).
[67] Zeeman energy corresponding to the $1s_{1/2} \rightarrow 2p_{3/2}$ transition or $1s_{1/2} \rightarrow 3d_{5/2}$ transition is 1.5 or 0.179 meV, much less than the corresponding transition energy, thus the perturbation theory is valid.
[68] K. Saitoh, Y. Hasegawa, N. Tanaka, and M. Uchida, J. Electron Microsc. **61**, 171 (2012).
[69] V. Grillo, G. C. Gazzadi, E. Mafakheri, S. Frabboni, E. Karimi, and R. W. Boyd, Phys. Rev. Lett. **114**, 034801 (2015).
[70] E. Mafakheri, A. H. Tavabi, P.-H. Lu, R. Balboni, F. Venturi, C. Menozzi, G. C. Gazzadi, S. Frabboni, A. Sit, R. E. Dunin-Borkowski, E. Karimi, and V. Grillo, Appl. Phys. Lett. **110**, 093113 (2017).
[71] B. J. McMorran, A. Agrawal, P. A. Ercius, V. Grillo, A. A. Herzing, T. R. Harvey, M. Linck, and J. S. Pierce, Phil. Trans. Roy. Soc. Lond. A **375**, 20150434 (2017).
[72] B. G. Mendis, Ultramicroscopy **157**, 1 (2015).
[73] T. Gericke, P. Würtz, D. Reitz, T. Langen, and H. Ott, Nat. Phys. **4**, 949 (2008); V. Guarrera and H. Ott, Adv. Imaging Electron Phys. **169**, 75 (2011); T. Manthey, T. M. Weber, T. Niederprüm, P. Langer, V. Guarrera, G. Barontini, and H. Ott, New J. Phys. **16**, 083034 (2014).
[74] H. J. Wang and W. Jhe, Phys. Rev. A **66**, 023610 (2002); H. J. Wang, X. X. Yi, X. W. Ba, and C. P. Sun, *ibid.* **64**, 043604 (2001).